



Incoherent broadband mid-infrared detection with lanthanide nanotransducers

Liangliang Liang^{1,6}✉, Chongwu Wang^{2,6}, Jiaye Chen¹, Qi Jie Wang^{2,3}✉ and Xiaogang Liu^{1,4,5}✉

Spectral conversion of mid-infrared (MIR) radiation to visible (VIS) and near-infrared (NIR) wavelengths is a fundamental technology for spectroscopy and imaging; however, current MIR-to-VIS/NIR conversion technology is limited to nonlinear optics with bulky crystals or resonant nanocavities. Here we report lanthanide-based MIR-to-NIR nanotransducers that enable broadband MIR sensing at room temperature by harnessing ratiometric luminescence changes. The ratiometric luminescence of lanthanide nanotransducers in the NIR region can be incoherently modulated by MIR radiation in the 4.5–10.8 μm wavelength range. Ratiometric modulation of luminescence enables a detection limit of $\sim 0.3 \text{ nW} \times \mu\text{m}^{-2}$ with an internal quantum efficiency on the order of 3×10^{-3} . The ratiometric sensor based on lanthanide nanotransducers does not require cryogenic cooling, polarization control, phase matching or nanoantenna design for light confinement. We also developed a camera with lanthanide nanotransducers, which enable room-temperature MIR imaging. We anticipate that these lanthanide nanotransducers can be extended to MIR light manipulation at the microscale for chip-integrated device applications.

Mid-infrared (MIR) spectroscopy has broad applications in the life sciences, remote sensing, security, industrial imaging and environmental monitoring^{1–5}. For instance, MIR spectroscopy enables structure determination of biological molecules and direct probing of almost all gas molecules⁶. It is also a powerful tool for optical communication in free space⁷. Despite tremendous efforts, the development of simple, low-cost and low-noise systems for room-temperature MIR detection and imaging still leaves much space for improvement^{8,9}. An alternative approach is to convert radiation from MIR to visible (VIS) and near-infrared (NIR) regions, which can be conveniently detected and imaged with silicon photodetectors due to their high sensitivity, cost-effectiveness and ease of integration. However, bulky nonlinear crystals are usually used to achieve spectral conversion, which require delicate polarization control, phase matching and a high-power pump laser^{10–14}. Consequently, nonlinear conversion requires high optical precision and mechanical stability, resulting in costly and complex instrumentation. Coherent detection of MIR radiation has recently been reported by surface-enhanced Raman scattering in optomechanical double-resonance nanocavities^{15,16}. However, this nanocavity approach requires sophisticated design and fabrication and works only in a narrow wavelength range as molecules with simultaneous Raman and infrared-active vibrations are required.

Lanthanide nanophosphors exhibit unique optical properties—including rich energy levels, long luminescence lifetimes, programmable emission bands and high photostability—and have found applications in super-resolution imaging, lasing and optogenetics^{17–26}. Here we report a new class of optical transducers based on lanthanide nanocrystals that enable incoherent broadband MIR sensing under ambient conditions by exploiting ratiometric NIR luminescence changes. Ratiometric measurements are generally insensitive to scattered light and instrumental fluctuations²⁷.

The basic experimental set-up includes a continuous-wave (CW) pump laser and lanthanide nanocrystals with quasi-continuous energy distribution (Fig. 1). Upon CW-MIR co-radiation, the intensity ratio of the two emission bands of the lanthanide nanotransducers can be modulated, which is the basic mechanism for MIR detection. Considering the low lattice phonon energy, hexagonal core-shell NaYF₄ nanocrystals doped with neodymium emitters (NaYF₄:Nd³⁺@NaYF₄) were selected as nanotransducers (Supplementary Fig. 1a–c). Nd³⁺ ions can be effectively pumped to the ⁴F_{7/2} state using a 740 nm CW laser, producing two Stokes emission bands centred at 806 nm (⁴F_{5/2} → ⁴I_{9/2}) and 866 nm (⁴F_{3/2} → ⁴I_{9/2}) (Fig. 1b and Supplementary Fig. 1d). The optimal doping concentration for bright nanotransducers is around 5% (Supplementary Fig. 2a).

Notably, the 806 nm emission band is much weaker than its 866 nm counterpart, which can be attributed to the rapid, multiphonon-assisted, non-radiative depopulation of ⁴F_{5/2} to the underlying ⁴F_{3/2} level (Fig. 1). Benefiting from the ultralong luminescence lifetime (tens to hundreds of microseconds) of the metastable ⁴F_{3/2} state (Supplementary Fig. 2b), efficient MIR back-pumping from the long-lived ⁴F_{3/2} level to higher energy levels (⁴F_{5/2}, ⁴F_{7/2}) can occur, leading to an additional population of the ⁴F_{5/2} level while depopulating the ⁴F_{3/2} level, thereby greatly increasing the 806/866 nm intensity ratio. It should be mentioned that spin-orbital coupling (*L*–*S* coupling) of lanthanide ions usually results in multiple densely packed energy levels, and the situation could be further facilitated by crystal field-induced splitting (Stark splitting), which allows quasi-continuous energy distribution^{28,29}. Nd³⁺-based nanotransducers therefore show a broadband response (~ 4 – $11 \mu\text{m}$) to MIR stimulation. Unlike nonlinear strategies for MIR transducing, transitions between real existing energy levels occur in lanthanide nanotransducers and are independent of polarization and phase matching. Consequently, these nanotransducers can

¹Department of Chemistry, National University of Singapore, Singapore, Singapore. ²Centre for OptoElectronics and Biophotonics, School of Electrical and Electronic Engineering, Nanyang Technological University, Singapore, Singapore. ³Centre for Disruptive Photonic Technologies, Division of Physics and Applied Physics School of Physical and Mathematical Sciences, Nanyang Technological University, Singapore, Singapore. ⁴Institute of Materials Research and Engineering, Agency for Science, Technology and Research, Singapore, Singapore. ⁵Center for Functional Materials, National University of Singapore Suzhou Research Institute, Suzhou, China. ⁶These authors contributed equally: Liangliang Liang, Chongwu Wang. ✉e-mail: chmliang@nus.edu.sg; qjwang@ntu.edu.sg; chmlx@nus.edu.sg

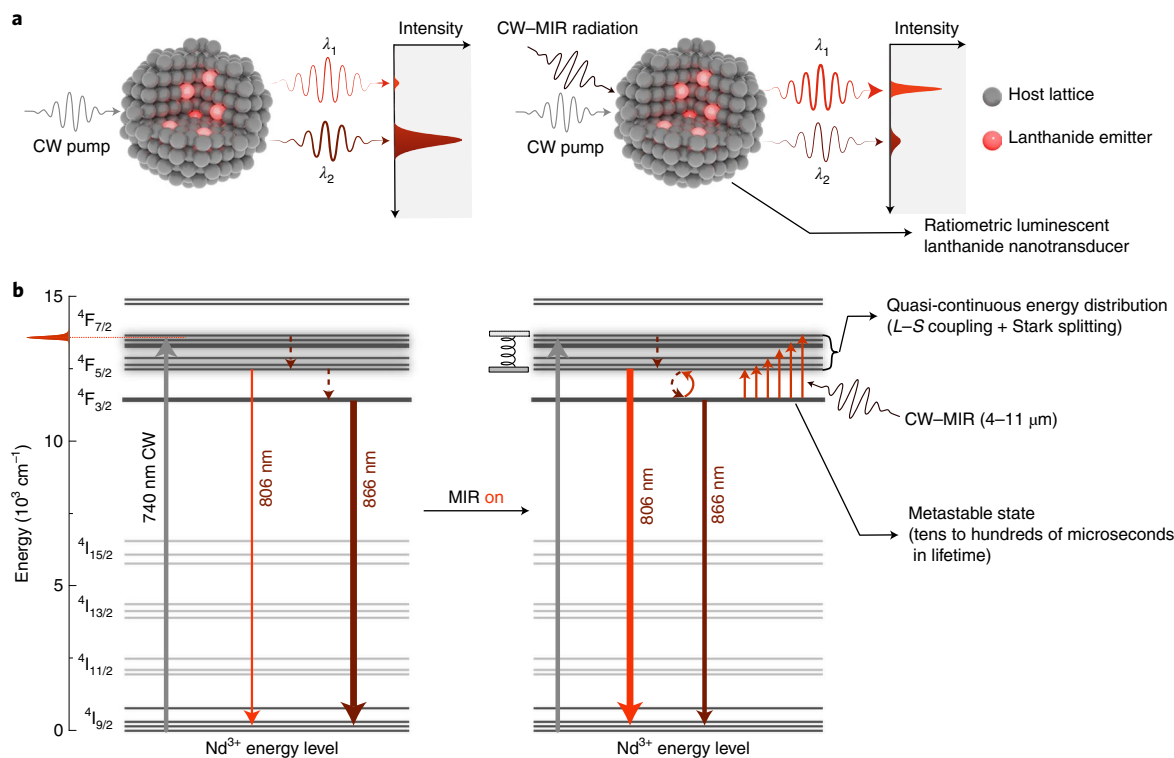


Fig. 1 | Mechanism of incoherent broadband MIR detection using lanthanide nanotransducers. **a**, Modulation of ratiometric luminescence of lanthanide nanotransducers under dual-CW-beam illumination (λ , wavelength). **b**, The working principle of broadband MIR sensing using Nd^{3+} -mediated nanotransducers. The incident CW-MIR beam induces substantial back-pumping of the long-lived metastable ${}^4\text{F}_{3/2}$ level to the higher ${}^4\text{F}_{7/2}$ level of Nd^{3+} . This leads to changes in the relative intensity of emission bands at 806 nm and 866 nm, and enables a ratiometric, time-resolved MIR sensor. Notably, a broadband ($\sim 4\text{--}11\ \mu\text{m}$) MIR measurement is enabled by a quasi-continuous energy distribution between the ${}^4\text{F}_{7/2}$ and ${}^4\text{F}_{5/2}$ levels of Nd^{3+} , arising from spin-orbital coupling ($L\text{--}S$ coupling) and crystal-field-induced splitting (Stark splitting).

be efficiently pumped even with a low-cost light-emitting diode, although a moderate absolute quantum yield of $\sim 10\%$ can be measured (Supplementary Fig. 2c).

To prove the concept, we used a simple fluorescence detection set-up to evaluate the response of prepared lanthanide nanotransducers to broadband MIR radiation (Fig. 2a). A transducer film with a thickness of $\sim 1\ \mu\text{m}$ was prepared by mounting $\sim 25\ \text{nm}$ $\text{NaYF}_4:\text{Nd}@/\text{NaYF}_4$ core-shell nanotransducers on a BaF_2 window (Supplementary Fig. 2d). The 740 nm excitation source and the MIR light from a quantum cascade laser (QCL) come from opposite directions and converge on the film. Any fluctuation in the ratiometric luminescence of nanotransducers was detected in real-time with a diffraction grating spectrometer.

Absorption of MIR radiation by the metastable ${}^4\text{F}_{3/2}$ state is the key step in modulating ratiometric luminescence. Additional broadband absorption occurred once a 740 nm pump beam was added during the Fourier-transform infrared (FTIR) measurement (Fig. 2b), signifying the relaying MIR absorption by the metastable ${}^4\text{F}_{3/2}$ state. For a film sample consisting of $\text{NaYF}_4:\text{Nd}(0.5\%)@/\text{NaYF}_4$ nanotransducers, a low peak ratio (806 nm/866 nm) of ~ 0.06 was measured when pumping with a 740 nm laser (Fig. 2c). Interestingly, this value increased to ~ 1.06 when MIR radiation was introduced at $8.1\ \mu\text{m}$ ($13\ \mu\text{W}\ \mu\text{m}^{-2}$). Although a temperature increase on the sample from 24 to 36.6°C was observed under our experimental conditions, the increase in the ratio caused by the thermal effect contributes less than 1% to the overall effect (Supplementary Fig. 3a,b). It is noteworthy that the thermal effect leads to an increase in both the 806 nm and 866 nm bands. By contrast, MIR co-radiation resulted in a drastic increase at 806 nm, but a decrease at 866 nm, suggesting that MIR radiation and the accompanying thermal effect

act simultaneously but differ to some extent in regulating the population of lanthanide energy levels (Supplementary Fig. 3c).

More importantly, the population kinetics of the metastable ${}^4\text{F}_{3/2}$ state largely determines the responsivity of nanotransducers to MIR radiation, as a more stable ${}^4\text{F}_{3/2}$ state has a greater probability of being pumped to higher energy levels by MIR radiation. Increasing the doping concentration of lanthanide emitters can generally trigger severe energy cross-relaxation, resulting in accelerated decay of the metastable state, as evidenced by the greatly shortened luminescence lifetime (Supplementary Fig. 2b)^{24,30,31}. A numerical simulation was performed based on a simplified energy model of Nd^{3+} emitters, where a larger cross-relaxation rate (k_{cro}) represents the case of a higher doping concentration (Supplementary Fig. 4a). The simulation results clearly show that less doping is more beneficial to improve the transducer's response to MIR radiation (Supplementary Fig. 4b). We next investigated the MIR-to-NIR transduction performance of nanotransducers with increasing Nd^{3+} doping concentrations (0.5, 5, 15 mol%). When we varied the pump power at 740 nm, we observed a linear dependence of the downshifting luminescence (Fig. 3a). Importantly, the ratio of peaks at 806 and 866 nm is independent of the pump power, regardless of the involvement of MIR radiation (Supplementary Fig. 5). The MIR-induced increase in the ratio is therefore not perturbed by the inevitable fluctuation in pump power (Fig. 3b), which is critical for high-precision detection. The increase in peak ratio scales linearly with the power of incident MIR radiation for all nanotransducers (Fig. 3c). In good agreement with theoretical simulations, nanotransducers with lower Nd^{3+} content responded more strongly to MIR radiation (Fig. 3b,c). Moreover, these Nd^{3+} -mediated nanotransducers showed a broadband ($4.5\text{--}10.8\ \mu\text{m}$) response to MIR stimulation (Fig. 3d).

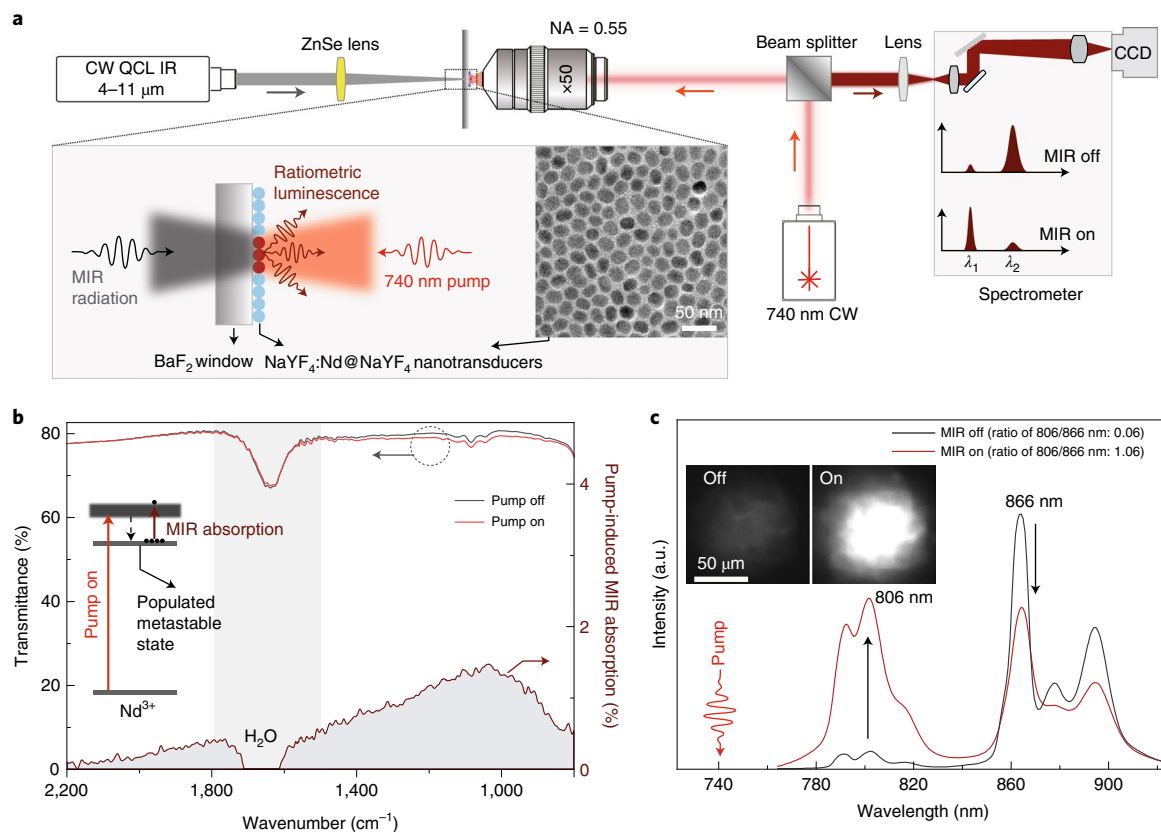


Fig. 2 | Ratiometric luminescence transduction from MIR radiation to the NIR region. **a**, Experimental set-up for MIR sensing. A 740 nm CW laser is used to pump the $\text{NaYF}_4\text{:Nd@NaYF}_4$ nanotransducer film, and a CW QCL is selected to provide the MIR radiation from 4 to 11 μm . **b**, FTIR spectra of the nanotransducer film with and without 740 nm laser pumping. The pump-induced MIR absorption (<1.5%) was determined from the difference between the two FTIR transmission spectra. **c**, Change in ratiometric luminescence of $\text{NaYF}_4\text{:Nd}$ (0.5%)@ NaYF_4 nanotransducers with and without MIR radiation (8.1 μm , 13 $\mu\text{W}\mu\text{m}^{-2}$). The acquisition time is 10 ms. The inset shows photographic images of the nanotransducer film before and after turning on the MIR laser, using an 800 nm bandpass filter. The acquisition time for the images is 3 ms. NA, numerical aperture. CCD, charge-coupled device.

For $\text{NaYF}_4\text{:Nd}(0.5\%)\text{@NaYF}_4$ nanotransducers, a sensitivity of more than $100\% \mu\text{W}^{-1} \mu\text{m}^2$ was measured at 8–9 μm MIR radiation. These lanthanide nanotransducers can reliably detect incident MIR power densities below $10 \text{ nW}\mu\text{m}^{-2}$ with a detection limit of $\sim 0.3 \text{ nW}\mu\text{m}^{-2}$ (Fig. 3e). However, without ratiometric detection, an impaired detection limit of $3.5 \text{ nW}\mu\text{m}^{-2}$ was measured by monitoring the intensity of the 806 nm band (Supplementary Fig. 6). To quantitatively analyse the MIR response of the nanotransducer, the NIR emissions around 806 nm were collected by a silicon photodetector. The recorded photovoltages for various MIR frequencies are shown in Fig. 3f, from which the external and internal quantum efficiencies for MIR-to-NIR were measured on the order of 3×10^{-5} and 3×10^{-3} , respectively, for the 806 nm band at 8.1 μm radiation, which can be attributed to efficient incoherent transduction (Fig. 3f).

Importantly, these lanthanide nanotransducers exhibit excellent long-term photostability (Fig. 4a). Upon high-power pumping at 740 nm and MIR co-irradiation, the peak ratio of a fixed spot on the transducer film shows no decline even after 2 h, despite slight fluctuations due to the power instability of the QCL laser source (<1%). Furthermore, lanthanide nanotransducers show strong resistance to perturbations resulting from temperature fluctuations in the environment and the surrounding infrared radiation (Supplementary Fig. 7). The wide wavelength response of the lanthanide nanotransducers can be applied for MIR spectroscopy, which records the vibrational pattern of molecules (known as fingerprints) at distinctive frequencies. As a proof of concept, we measured the absorption spectra for a multicomponent mixture of CH_4 , SO_2 , and water

vapour from 1,290 to 1,670 cm^{-1} . The MIR light passes through a 10 cm gas cell filled with the target or reference gases (nitrogen gas), and is then focused on the nanotransducer film (Fig. 4b). The light attenuation by gas molecules diluted in nitrogen can be well recorded by monitoring both the intensity fluctuation at 806 nm and the 806/866 nm ratio. It can be found that the absorption peaks for each component match well with the simulation from the HITRAN database when the 806 nm emission band was used to monitor the MIR light absorption³². Importantly, when the ratiometric strategy is used, perturbation due to fluctuation in excitation power can be well eliminated to further improve the detection limit (Supplementary Fig. 8).

We next used lanthanide nanotransducers to demonstrate a proof of concept for room-temperature MIR imaging using a low-cost CMOS camera (Fig. 4c,d). A MIR light source was projected onto the transducer film using a ZnSe lens. The light intensity distribution on the film was directly imaged by recording the transduced NIR emission intensity around 800 nm with the CMOS camera (Fig. 4c). A punch-out letter plate illuminated with a 7.3 μm CW-MIR laser was imaged well with an integration time of 2 ms (Fig. 4d). Although the imaging performance of the currently developed lanthanide nanotransducers is inferior to that of commercial MIR cameras based on InSb or HgCdTe semiconductors, which are normally operated at low temperatures (Supplementary Table 1), the imaging quality can be improved by developing much brighter and more MIR-sensitive lanthanide nanotransducers, or by fabricating more uniform nanotransducer films.

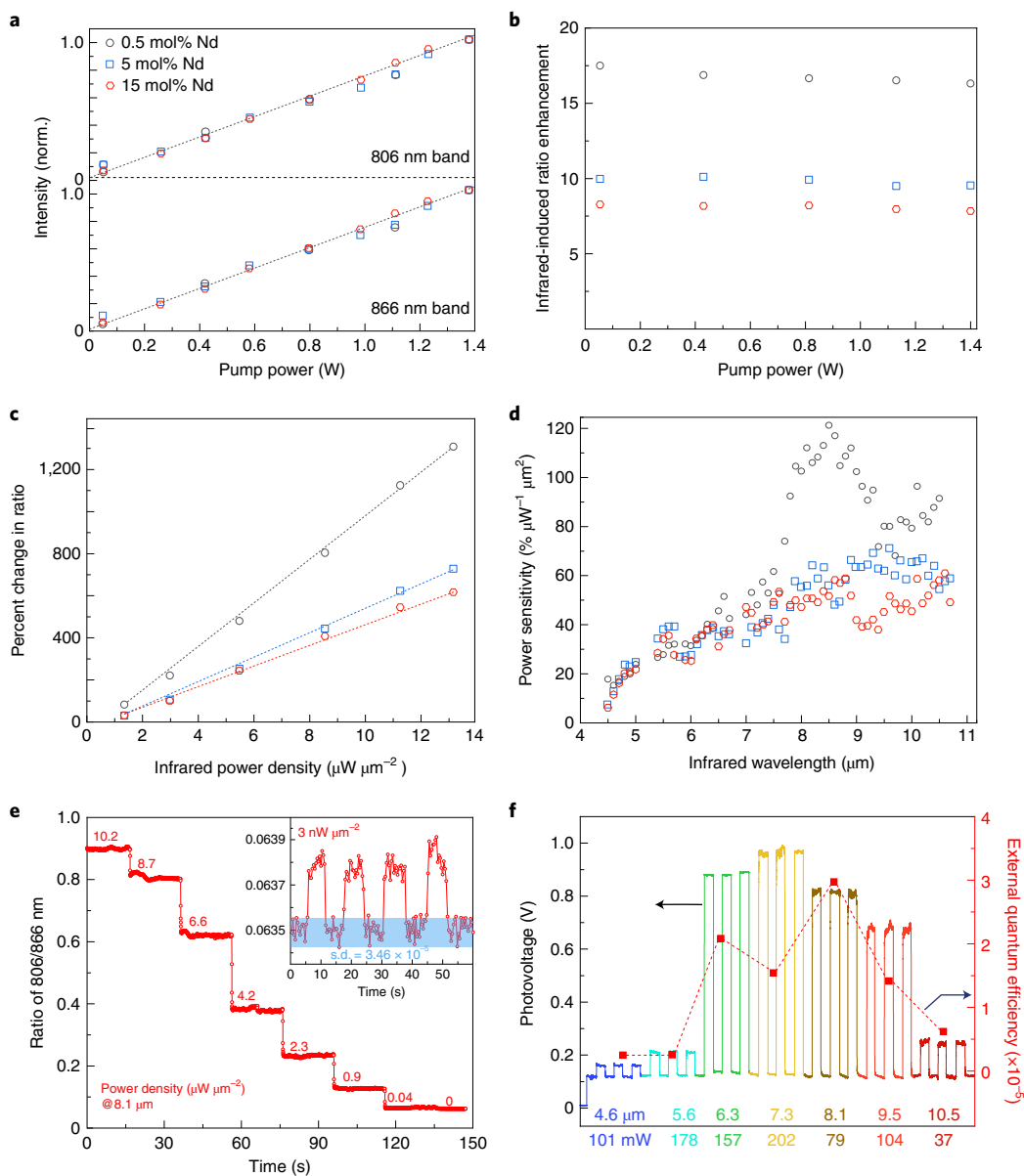


Fig. 3 | Response of ratiometric luminescent nanotransducers to MIR stimulation. **a**, Power dependence for the downshifting emission bands at 806 nm and 866 nm as a function of pump power and doping concentration of the Nd³⁺ transducers. **b**, MIR radiation-induced increase in luminescence ratio for transducers activated with varied Nd³⁺ concentrations as a function of pump power (MIR power 13 $\mu\text{W } \mu\text{m}^{-2}$, tuned at 8.1 μm). **c**, Power dependence of the MIR beam (8.1 μm) on the percent change in ratio for different Nd³⁺ nanotransducers. **d**, Ratiometric broadband MIR (from 4.5 to 10.8 μm) detection sensitivity of different Nd³⁺ nanotransducers. **e**, Detection limit measurement for a MIR radiance of 8.1 μm using NaYF₄:Nd(0.5%)@NaYF₄ nanotransducers. With a signal-to-noise ratio of 1, the equivalent MIR power density at 8.1 μm is estimated to be 0.3 nW μm^{-2} . The averaging times are 40 ms (main graph) and 400 ms (inset). **f**, Photovoltage of a silicon photodetector collecting 806 nm emission at various MIR wavelength radiation using NaYF₄:Nd(0.5%)@NaYF₄ nanotransducers, as well as the calculated external quantum efficiency for conversion of MIR radiation to the 806 nm emission band. An internal quantum efficiency of $\sim 3 \times 10^{-3}$ at 8.1 μm can be calculated as $\sim 1\%$ of the incident MIR light was absorbed by the transducer film. The values at the bottom of the figure refer to the power at the corresponding MIR wavelength.

The development of ratiometric luminescent nanotransducers provides new possibilities for low-cost, high-efficiency MIR sensing and imaging under ambient conditions. The transduction performance of lanthanide nanotransducers could be further improved through optical engineering and rational design of nanocrystal structures. For instance, a resonant cavity could be implemented to increase the quantum efficiency of optical transducers through enhanced light-matter interactions³³. Furthermore, incorporation of energy transfer into lanthanide nanotransducers may further improve the sensitivity of ratiometric luminescence to MIR modulation³⁴,

and the toolbox of lanthanide nanotransducers could be expanded by employing other lanthanide emitters with an extended spectral response in the MIR range and better detection performance. From the fundamental research perspective, the involvement of lanthanide nanotransducers provides the academic community with a useful toolbox for light manipulation in the MIR region, and these optical nanotransducers could also find stimulating applications in nanophotonics. For example, lanthanide nanotransducers offer high flexibility in large and microscale patterning through inkjet printing³⁵, which has tremendous potential for MIR-integrated photonics.

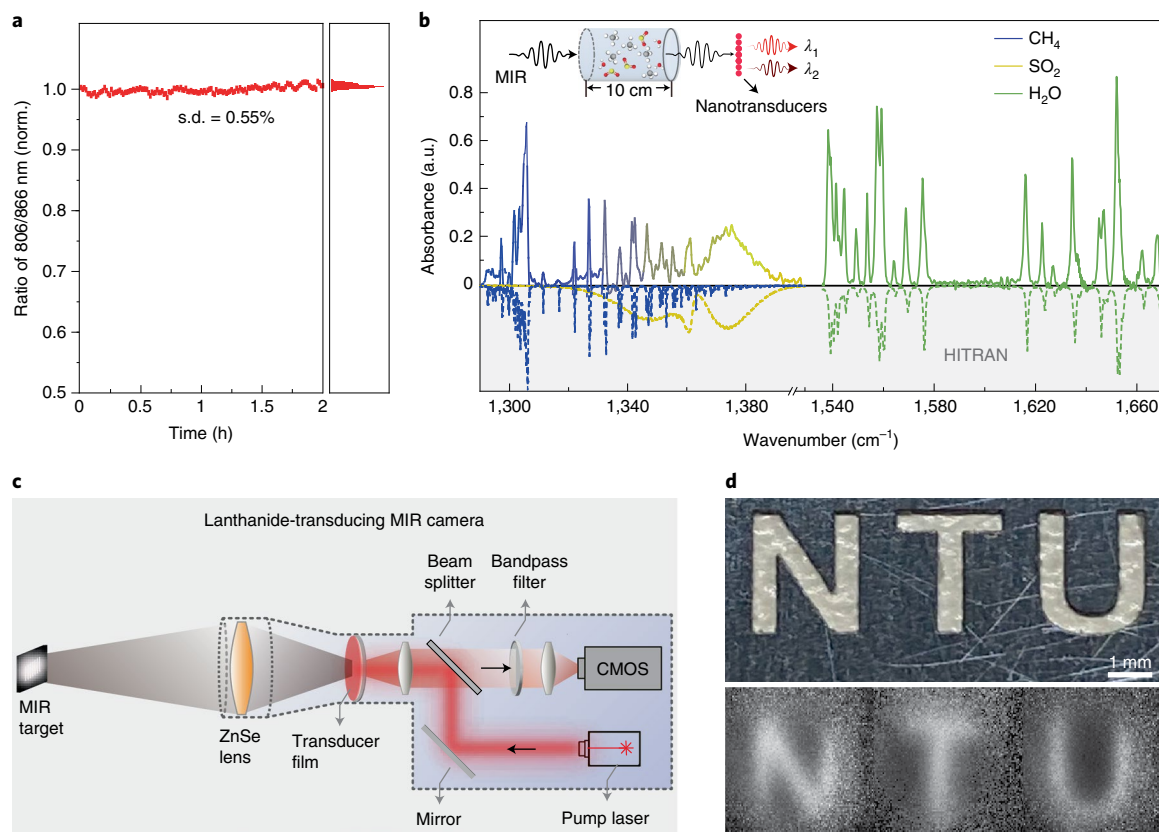


Fig. 4 | Proof-of-concept for lanthanide nanotransducer-mediated broadband gas sensing and room-temperature MIR imaging with a CMOS camera.

a, Photostability test performed by monitoring the ratio of 806/866 nm emissions under co-illumination with 740 nm (1.4 W) and 8.1 μm (79.4 mW) CW lasers for 2 h. **b**, Multicomponent gas sensing for a mixture of CH_4 (0.8%), SO_2 (0.2%) and H_2O (2%) in a 10 cm gas cell using neodymium nanotransducers. **c**, Lanthanide transducer camera configuration for MIR imaging at room temperature. **d**, MIR imaging (7.3 μm) of a punch-out letter plate using transduced NIR emission (806 nm band) captured by a CMOS camera. The integration time for each image frame is 2 ms.

Online content

Any methods, additional references, Nature Research reporting summaries, source data, extended data, supplementary information, acknowledgements, peer review information; details of author contributions and competing interests; and statements of data and code availability are available at <https://doi.org/10.1038/s41566-022-01042-7>.

Received: 2 March 2022; Accepted: 21 June 2022;

Published online: 01 August 2022

References

- Waynant, R. W., Ilev, I. K. & Gannot, I. Mid-infrared laser applications in medicine and biology. *Philos. Trans. R. Soc. A* **359**, 635–644 (2001).
- Ouzounov, D. & Freund, F. Mid-infrared emission prior to strong earthquakes analyzed by remote sensing data. *Adv. Space Res.* **33**, 268–273 (2004).
- Tittel, F. K. et al. in *Terahertz and Mid Infrared Radiation: Detection of Explosives and CBRN (Using Terahertz)* 153–165 (Springer, 2014).
- Ring, E. Beyond human vision: the development and applications of infrared thermal imaging. *Imaging Sci. J.* **58**, 254–260 (2010).
- de Cumis, M. S. et al. Widely-tunable mid-infrared fiber-coupled quartz-enhanced photoacoustic sensor for environmental monitoring. *Opt. Express* **22**, 28222–28231 (2014).
- Du, Z., Zhang, S., Li, J., Gao, N. & Tong, K. Mid-infrared tunable laser-based broadband fingerprint absorption spectroscopy for trace gas sensing: a review. *Appl. Sci.* **9**, 338 (2019).
- Roellig, T. L. et al. Mid-infrared detector development for the Origins Space Telescope. *J. Astron. Telesc. Instrum. Syst.* **6**, 041503 (2020).
- Rogalski, A. Infrared detectors: an overview. *Infrared Phys. Technol.* **43**, 187–210 (2002).
- Stuart, B. H. *Infrared Spectroscopy: Fundamentals and Applications* (Wiley, 2004).
- Temporão, G. et al. Mid-infrared single-photon counting. *Opt. Lett.* **31**, 1094–1096 (2006).
- Dam, J. S., Tidemand-Lichtenberg, P. & Pedersen, C. Room-temperature mid-infrared single-photon spectral imaging. *Nat. Photon.* **6**, 788–793 (2012).
- Tseng, Y.-P., Pedersen, C. & Tidemand-Lichtenberg, P. Upconversion detection of long-wave infrared radiation from a quantum cascade laser. *Opt. Mater. Express* **8**, 1313–1321 (2018).
- Ashik, A. et al. Mid-infrared upconversion imaging using femtosecond pulses. *Photon. Res.* **7**, 783–791 (2019).
- Mancinelli, M. et al. Mid-infrared coincidence measurements on twin photons at room temperature. *Nat. Commun.* **8**, 1–8 (2017).
- Chen, W. et al. Continuous-wave frequency upconversion with a molecular optomechanical nanocavity. *Science* **374**, 1264–1267 (2021).
- Xomalis, A. et al. Detecting mid-infrared light by molecular frequency upconversion in dual-wavelength nanoantennas. *Science* **374**, 1268–1271 (2021).
- Wegh, R. T., Donker, H., Oskam, K. D. & Meijerink, A. Visible quantum cutting in $\text{LiGdF}_4:\text{Eu}^{3+}$ through downconversion. *Science* **283**, 663–666 (1999).
- Liu, Y. et al. Amplified stimulated emission in upconversion nanoparticles for super-resolution nanoscopy. *Nature* **543**, 229–233 (2017).
- Lee, C. et al. Giant nonlinear optical responses from photon-avalanching nanoparticles. *Nature* **589**, 230–235 (2021).
- Fernandez-Bravo, A. et al. Continuous-wave upconverting nanoparticle microlasers. *Nat. Nanotechnol.* **13**, 572–577 (2018).
- Liang, L. et al. Continuous-wave near-infrared stimulated-emission depletion microscopy using downshifting lanthanide nanoparticles. *Nat. Nanotechnol.* **16**, 975–980 (2021).
- Chen, S. et al. Near-infrared deep brain stimulation via upconversion nanoparticle-mediated optogenetics. *Science* **359**, 679–684 (2018).

23. Bünzli, J.-C. G. & Piguet, C. Taking advantage of luminescent lanthanide ions. *Chem. Soc. Rev.* **34**, 1048–1077 (2005).
24. Malta, O. L. & Carlos, L. D. Intensities of $4f-4f$ transitions in glass materials. *Quim. Nova* **26**, 889–895 (2003).
25. Walsh, B. M., Lee, H. R. & Barnes, N. P. Mid infrared lasers for remote sensing applications. *J. Lumin.* **169**, 400–405 (2016).
26. Cadatal-Raduban, M. et al. Mid-infrared imaging through up-conversion luminescence in trivalent lanthanide ion-doped self-organizing optical fiber array crystal. *Opt. Lett.* **46**, 941–944 (2021).
27. Park, S.-H., Kwon, N., Lee, J.-H., Yoon, J. & Shin, I. Synthetic ratiometric fluorescent probes for detection of ions. *Chem. Soc. Rev.* **49**, 143–179 (2020).
28. Smentek, L. Theoretical description of the spectroscopic properties of rare earth ions in crystals. *Phys. Rep.* **297**, 155–237 (1998).
29. Dorenbos, P. The $4f^n \leftrightarrow 4f^{n-1} 5d$ transitions of the trivalent lanthanides in halogenides and chalcogenides. *J. Lumin.* **91**, 91–106 (2000).
30. Danielmeyer, H., Blätte, M. & Balmer, P. Fluorescence quenching in Nd:YAG. *Appl. Phys.* **1**, 269–274 (1973).
31. Chen, G. et al. Core/shell NaGdF₄:Nd³⁺/NaGdF₄ nanocrystals with efficient near-infrared to near-infrared downconversion photoluminescence for bioimaging applications. *ACS Nano* **6**, 2969–2977 (2012).
32. Gordon, I. E. et al. The HITRAN2020 molecular spectroscopic database. *J. Quant. Spectrosc. Radiat. Transf.* **277**, 107949 (2022).
33. Dam, J. S., Pedersen, C. & Tidemand-Lichtenberg, P. High-resolution two-dimensional image upconversion of incoherent light. *Opt. Lett.* **35**, 3796–3798 (2010).
34. Dong, H., Sun, L.-D. & Yan, C.-H. Energy transfer in lanthanide upconversion studies for extended optical applications. *Chem. Soc. Rev.* **44**, 1608–1634 (2015).
35. Liu, H. et al. Tunable resonator-upconverted emission (TRUE) color printing and applications in optical security. *Adv. Mater.* **31**, 1807900 (2019).

Publisher's note Springer Nature remains neutral with regard to jurisdictional claims in published maps and institutional affiliations.

© The Author(s), under exclusive licence to Springer Nature Limited 2022

Methods

Materials. Sodium hydroxide (NaOH; >98%), ammonium fluoride (NH₄F; >98%), 1-octadecene (90%), oleic acid (90%), yttrium acetate hydrate (Y(CH₃CO₂)₃·xH₂O; 99.9%), neodymium acetate hydrate (Nd(CH₃CO₂)₃·xH₂O; 99.9%), cyclohexane (>98%) and methanol (>99%) were all purchased from Sigma-Aldrich and used as received without further purification.

Preparation of lanthanide nanotransducers. Specially designed Nd³⁺-doped nanocrystals were synthesized by a modified co-precipitation method³⁶. In a typical procedure, an aqueous solution (4 ml) of Nd(CH₃CO₂)₃ and Y(CH₃CO₂)₃ in various molar ratios ($x/100 - x$, where $x = 0.5, 5, 15$) was added to a 50 ml flask containing 6.0 ml of oleic acid and 14 ml of 1-octadecene. The mixture was heated to 150 °C and kept for 60 min to form lanthanide-oleate coordination complexes. After cooling down to 50 °C, a methanol solution (12 ml) containing NH₄F (3.2 mmol) and NaOH (2.0 mmol) was added under stirring at 50 °C for 60 min. The solution was then heated to 100 °C and kept under vacuum for 20 min to remove the volatile residue. The remaining mixture was heated to 290 °C and maintained at this temperature for 3 h under an inert nitrogen environment. After cooling to room temperature, the resulting nanocrystals were collected by centrifugation, washed several times with ethanol, and dispersed in 4 ml of cyclohexane for further treatment. To synthesize neodymium-activated core-shell nanocrystals, a shell precursor containing 0.8 mmol Y(CH₃CO₂)₃ was prepared following the procedure described above. The as-synthesized core nanocrystals were added to the shell precursor and kept at 80 °C for 40 min. When the resultant mixture was cooled to 50 °C, a methanol solution (12 ml) of NH₄F (3.2 mmol) and NaOH (2 mmol) was added. After further stirring for 30 min at 50 °C, the reaction was heated to 100 °C and then the impurities were pumped off, followed by further heating to 290 °C. After the reaction was completed after 2 h, the as-synthesized core-shell nanocrystals were washed with ethanol and then dispersed in 4 ml cyclohexane. To remove surface ligands of lanthanide nanotransducers, neodymium-doped core-shell nanocrystals dispersed in cyclohexane (1 ml, 0.2 M) were first precipitated by adding 4 ml of ethanol. The solid was collected by centrifugation and redispersed in 1 ml ethanol. After the addition of 1 ml HCl solution (2 mol l⁻¹), the mixture was sonicated for several seconds and then centrifuged. Ligand-free nanocrystals were redispersed in 1 ml of ethanol for further use³⁷. Lanthanide nanotransducer films were prepared using a simple drop-casting method. Specifically, 20 μl of ethanol solution containing ligand-free nanotransducers (10 mg ml⁻¹) was dropped onto a BaF₂ substrate (5 mm thick) placed in a Petri dish. The sample was kept immobile and the Petri dish was covered to reduce the evaporation rate and thus the number of cracks.

Optical set-up and data acquisition. A home-built fluorescence detection system was used to investigate the response of prepared lanthanide nanotransducers to MIR radiation. A multimode laser with a wavelength of 740 nm (CNI-MDL-III) was used for excitation. The light was reflected by a 760 nm dichroic long-pass filter (Newport HPD760, Newport) and focused on the nanotransducer film through a ×50 objective (Mitutoyo, NA = 0.55). For the introduction of the MIR source, a QCL with a power tuning of 4.4 to 10.8 μm (Daylight Solutions, MIRcat) was used, and the light beam was focused on the nanotransducer film using a ZnSe lens with a focal length of 5 cm (Thorlabs). For data collection of ratiometric luminescence, a 750 nm long-pass filter was placed between the dichroic filter and a lens to focus the emission onto the fibre end of a grating spectrometer (Ocean optics, QE Pro). The integration time used for spectrum acquisition is 10 ms. Furthermore, the real-time peak ratio between 806 nm and 866 nm can be obtained using the peak ratio collection mode of the spectrometer. The limit of detection (LOD) is defined in terms of signal value at which a signal-to-noise ratio is one, and the standard deviation of the response curve is used to derive the detection limit. The LOD is calculated by the equation: LOD = standard deviation/slop, in which the standard deviation stands for the standard deviation of the infrared off signal (806 nm emission or the ratio of 806/866), the slop is derived from the linear fitting for the curve of power-dependent infrared response.

The emission power can be detected and measured with a silicon-amplified detector (Thorlabs, PDA36A2). The gain was set to 60 dB, corresponding to a responsivity of 7.5×10^5 V W⁻¹. The 800 nm bandpass filter (Thorlabs, FBH800-40) was placed in front of the detector to filter the emission around 800 nm. The output voltage was connected to a high-sensitivity digital source meter (Keysight, 2912 A). For single-band (806 nm) power-dependent photoresponse measurements, the infrared emission was modulated with an optical chopper at 15 Hz. The output voltage was demodulated with a time constant of 100 ms using a lock-in amplifier (Zurich Instruments, HF2LI). The MIR laser power was measured using a thermal power meter (OPHIR, Nova display-ROHS).

For the measurement of MIR transduction efficiency, the power of the enhanced emission around 806 nm was recorded with an amplified silicon detector (Thorlabs, PDA36A2). Considering the transmission of the objective (65%), dichroic filter (89%) and lens (91%), an overall collection efficiency of less than 4% can be estimated. The following expression was used to calculate external and internal quantum efficiencies for MIR-to-NIR transduction. The absorption of MIR light by the transducer film was measured by the FTIR spectroscopy with and without the 740 nm pump laser.

$$\eta_{\text{External}} = \frac{\text{Power}_{\text{NIR}}/(h\nu_{\text{NIR}})}{\text{Power}_{\text{MIR input}}/(h\nu_{\text{MIR}})}$$

$$\eta_{\text{Internal}} = \frac{\text{Power}_{\text{NIR}}/(h\nu_{\text{NIR}})}{\text{Power}_{\text{MIR absorbed}}/(h\nu_{\text{MIR}})}$$

For MIR imaging demonstration, a QCL CW-MIR laser working at 7.3 μm was used as the light source, and a micrometre-sized pattern was placed in front of it to obtain a patterned light source. Then the light was projected through a ZnSe lens onto a lanthanide nanotransducer film. A CMOS camera (Thorlabs, CS135MUN) behind the film was used to record the emission pattern of the transducer film. An 800 nm bandpass filter (Thorlabs, FBH800-40) was used to extract the transduced emission. To achieve MIR imaging using the emission intensity at 806 nm, the background images were first taken with (MIR on) and without (MIR off) the MIR radiation; the sample was then placed on the MIR light path and an image was captured (sample). To extract the contrast information of the sample, the following algorithm was used.

$$\text{Contrast} = \frac{\text{Sample} - \text{MIR off}}{\text{MIR on} - \text{MIR off}}$$

For gas sensing demonstration, a gas cell with an optical length of 10 cm was placed in the infrared optical path and filled with a reference (N₂) or target gas (CH₄ (0.8%), SO₂ (0.2%), H₂O (2%)). The intensity of transmitted MIR light after passing through the gas cell was then collected by recording the emission intensity at 806 nm using a photodetector and/or the 806/866 nm intensity ratio using a grating spectrometer (Ocean optics, QE Pro). For the single-band sensing (806 nm), the infrared emission was modulated with an optical chopper at 15 Hz. The output voltage was demodulated with a time constant of 100 ms using a lock-in amplifier (Zurich Instruments, HF2LI). The wavenumber of the QCL source was scanned 30 times from 1,290 to 1,670 cm⁻¹. Absorption spectra were calculated using the Beer-Lambert law (that is, absorbance = $-\log_{10}(I_{\text{gas}}/I_{\text{ref}})$) and the concentration for each component was derived using the standard spectra from the HITRAN database.

Numerical simulation of the MIR modulation process. The population distribution at the different energy levels of neodymium emitters can be well simulated with and without the MIR radiation (Supplementary Fig. 5). Here we build a simplified model in which only important transition steps are considered. As the cross-relaxation process can be facilitated with higher doping concentration, varied cross-relaxation rates are used here to study the performance of transducers with different doping contents. Moreover, only downshifting processes are involved in this model, and minor upconversion processes are ignored; we therefore applied the following rate equations for a typical simplified neodymium transducer system:

$$\frac{d(n_{E1})}{dt} = -P_{\text{pump}} \frac{\lambda_{\text{pump}}}{hc} \sigma_{\text{pump}} E_1 - k_{\text{cro}} E_1 E_3 + k_{21} E_2 + k_{41} E_4 + k_{31} E_3; \quad (1)$$

$$\frac{d(n_{E2})}{dt} = 2k_{\text{cro}} E_1 E_3 - k_{21} E_2; \quad (2)$$

$$\frac{d(n_{E3})}{dt} = -k_{\text{cro}} E_1 E_3 + k_{43} E_4 - k_{31} E_3 - P_{\text{MIR}} \frac{\lambda_{\text{MIR}}}{hc} \sigma_{\text{MIR}} E_3; \quad (3)$$

$$\frac{d(n_{E4})}{dt} = k_{54} E_5 - k_{43} E_4 - k_{41} E_4 + P_{\text{MIR}} \frac{\lambda_{\text{MIR}}}{hc} \sigma_{\text{MIR}} E_3; \quad (4)$$

$$\frac{d(n_{E5})}{dt} = P_{\text{pump}} \frac{\lambda_{\text{pump}}}{hc} \sigma_{\text{pump}} E_1 - k_{54} E_5; \quad (5)$$

In these equations, P_{pump} and P_{MIR} are the power densities of the pump and incident MIR beams, respectively; h and c are the Planck constant and the speed of light in vacuum, respectively; σ_{pump} and σ_{MIR} are the absorption cross-sections of the pump light and the MIR radiation of the lanthanide ion, respectively; n_{E_i} is the population of energy level, E_i ; k_{ij} is the relaxation decay rate from E_i to E_j ; and k_{cro} is the cross-relaxation rate. The differential equation system was solved using Mathematica 12.0 and 1stOpt 9.0 program from 7D Soft High Technology³⁸.

Reporting summary. Further information on research design is available in the Nature Research Reporting Summary linked to this article.

Data availability

All relevant data that support the findings of this work are available from the corresponding author on reasonable request. Source Data are provided with this paper.

Code availability

The Mathematica and 1stOpt-based codes for theoretical modelling and numerical simulations are available from the corresponding author on reasonable request.

References

36. Wang, F. et al. Simultaneous phase and size control of upconversion nanocrystals through lanthanide doping. *Nature* **463**, 1061–1065 (2010).
37. Tian, J. et al. Intracellular adenosine triphosphate deprivation through lanthanide-doped nanoparticles. *J. Am. Chem. Soc.* **137**, 6550–6558 (2015).
38. Wolfram Research, Inc., Mathematica, Version 13.1, Champaign, IL (2022).

Acknowledgements

This work was supported by the Singapore Ministry of Education (grant nos. MOE2017-T2-2-110 and MOE2016-T3-1-006(S)), the Agency for Science, Technology and Research (A*STAR) (grant nos. A1983c0038 and A2090b0144), and National Research Foundation, Prime Minister's Office, Singapore (award nos. NRF-NRFI05-2019-003, NRF-CRP18-2017-02, NRF-CRP22-2019-0002 and NRF-CRP19-2017-01).

Author contributions

L.L. and X.L. conceived the idea. X.L. and Q.J.W. supervised the project and led the collaborative efforts. L.L. designed the nanotransducers and conducted numerical simulations with contributions from J.C. L.L. and C.W. conducted optical experiments. L.L., C.W. and X.L. wrote the manuscript. All authors participated in the discussion and analysis of the manuscript.

Competing interests

The authors declare no competing interests.

Additional information

Supplementary information The online version contains supplementary material available at <https://doi.org/10.1038/s41566-022-01042-7>.

Correspondence and requests for materials should be addressed to Liangliang Liang, Qi Jie Wang or Xiaogang Liu.

Peer review information *Nature Nanotechnology* thanks Guanying Chen, Dayong Jin and the other, anonymous, reviewer(s) for their contribution to the peer review of this work.

Reprints and permissions information is available at www.nature.com/reprints.

Reporting Summary

Nature Portfolio wishes to improve the reproducibility of the work that we publish. This form provides structure for consistency and transparency in reporting. For further information on Nature Portfolio policies, see our [Editorial Policies](#) and the [Editorial Policy Checklist](#).

Statistics

For all statistical analyses, confirm that the following items are present in the figure legend, table legend, main text, or Methods section.

n/a Confirmed

- The exact sample size (n) for each experimental group/condition, given as a discrete number and unit of measurement
- A statement on whether measurements were taken from distinct samples or whether the same sample was measured repeatedly
- The statistical test(s) used AND whether they are one- or two-sided
Only common tests should be described solely by name; describe more complex techniques in the Methods section.
- A description of all covariates tested
- A description of any assumptions or corrections, such as tests of normality and adjustment for multiple comparisons
- A full description of the statistical parameters including central tendency (e.g. means) or other basic estimates (e.g. regression coefficient) AND variation (e.g. standard deviation) or associated estimates of uncertainty (e.g. confidence intervals)
- For null hypothesis testing, the test statistic (e.g. F , t , r) with confidence intervals, effect sizes, degrees of freedom and P value noted
Give P values as exact values whenever suitable.
- For Bayesian analysis, information on the choice of priors and Markov chain Monte Carlo settings
- For hierarchical and complex designs, identification of the appropriate level for tests and full reporting of outcomes
- Estimates of effect sizes (e.g. Cohen's d , Pearson's r), indicating how they were calculated

Our web collection on [statistics for biologists](#) contains articles on many of the points above.

Software and code

Policy information about [availability of computer code](#)

Data collection

Data analysis

For manuscripts utilizing custom algorithms or software that are central to the research but not yet described in published literature, software must be made available to editors and reviewers. We strongly encourage code deposition in a community repository (e.g. GitHub). See the Nature Portfolio [guidelines for submitting code & software](#) for further information.

Data

Policy information about [availability of data](#)

All manuscripts must include a [data availability statement](#). This statement should provide the following information, where applicable:

- Accession codes, unique identifiers, or web links for publicly available datasets
- A description of any restrictions on data availability
- For clinical datasets or third party data, please ensure that the statement adheres to our [policy](#)

Source data are provided with this paper. All relevant data that support the findings of this work are available from the corresponding author upon reasonable request.

Human research participants

Policy information about [studies involving human research participants and Sex and Gender in Research](#).

Reporting on sex and gender	<input type="text" value="N.A."/>
Population characteristics	<input type="text" value="N.A."/>
Recruitment	<input type="text" value="N.A."/>
Ethics oversight	<input type="text" value="N.A."/>

Note that full information on the approval of the study protocol must also be provided in the manuscript.

Field-specific reporting

Please select the one below that is the best fit for your research. If you are not sure, read the appropriate sections before making your selection.

Life sciences Behavioural & social sciences Ecological, evolutionary & environmental sciences

For a reference copy of the document with all sections, see [nature.com/documents/nr-reporting-summary-flat.pdf](https://www.nature.com/documents/nr-reporting-summary-flat.pdf)

Ecological, evolutionary & environmental sciences study design

All studies must disclose on these points even when the disclosure is negative.

Study description	<input type="text" value="Mid infrared light are detected using lanthanide-doped nanocrystals."/>
Research sample	<input type="text" value="lanthanide-doped nanoparticle film."/>
Sampling strategy	<input type="text" value="Samples with different doping concentration are investigated."/>
Data collection	<input type="text" value="The emission spectra were collected when samples are illuminated by NIR light and MIR light."/>
Timing and spatial scale	<input type="text" value="All data are collected between Nov.2021 and Mar.2022."/>
Data exclusions	<input type="text" value="N.A."/>
Reproducibility	<input type="text" value="Multiple samples are measured."/>
Randomization	<input type="text" value="All samples with different doping concentrations are systematically investigated."/>
Blinding	<input type="text" value="Blinding is not relevant to this study."/>

Did the study involve field work? Yes No

Reporting for specific materials, systems and methods

We require information from authors about some types of materials, experimental systems and methods used in many studies. Here, indicate whether each material, system or method listed is relevant to your study. If you are not sure if a list item applies to your research, read the appropriate section before selecting a response.

Materials & experimental systems

n/a	Involvement in the study
<input checked="" type="checkbox"/>	<input type="checkbox"/> Antibodies
<input checked="" type="checkbox"/>	<input type="checkbox"/> Eukaryotic cell lines
<input checked="" type="checkbox"/>	<input type="checkbox"/> Palaeontology and archaeology
<input checked="" type="checkbox"/>	<input type="checkbox"/> Animals and other organisms
<input checked="" type="checkbox"/>	<input type="checkbox"/> Clinical data
<input checked="" type="checkbox"/>	<input type="checkbox"/> Dual use research of concern

Methods

n/a	Involvement in the study
<input checked="" type="checkbox"/>	<input type="checkbox"/> ChIP-seq
<input checked="" type="checkbox"/>	<input type="checkbox"/> Flow cytometry
<input checked="" type="checkbox"/>	<input type="checkbox"/> MRI-based neuroimaging